Optical Dark-Field and Electron Energy Loss Imaging and Spectroscopy of Symmetry-Forbidden Modes in Loaded Nanogap Antennas

Todd Brintlinger,[†] Andrew A. Herzing,[‡] James P. Long,[§] Igor Vurgaftman,[∥] Rhonda Stroud,[†] and B. S. Simpkins*[,§]

[†]Materials Division, Naval Research Laboratory, 4555 Overlook Avenue SW, Washington, DC 20375, United States, [‡]Materials Measurement Laboratory, National Institute of Standards and Technology, Gaithersburg, Maryland 20899, United States, [§]Chemistry Division, Naval Research Laboratory, 4555 Overlook Avenue SW, Washington, DC 20375, United States, and [∥]Optical Sciences Division, Naval Research Laboratory, 4555 Overlook Avenue SW, Washington, DC 20375, United States

ABSTRACT We have produced large numbers of hybrid metal—semiconductor nanogap antennas using a scalable electrochemical approach and systematically characterized the spectral and spatial character of their plasmonic modes with optical dark-field scattering, electron energy loss spectroscopy with principal component analysis, and full wave simulations. The coordination of these techniques reveal that these nanostructures support degenerate transverse modes which split due to substrate interactions, a longitudinal mode which scales with antenna length, and a symmetry-forbidden *gap-localized transverse* mode. This gap-localized transverse mode arises from mode splitting of transverse resonances supported on both antenna arms and is confined to the gap load enabling (i) delivery of substantial energy to the gap material and (ii) the possibility of tuning the antenna resonance *via* active modulation of the gap material's optical properties. The resonant position of this symmetry-forbidden mode is sensitive to gap size, dielectric strength of the gap material, and is highly suppressed in air-gapped structures which may explain its absence from the literature to date. Understanding the complex modal structure supported on hybrid nanosystems is necessary to enable the multifunctional components many seek.

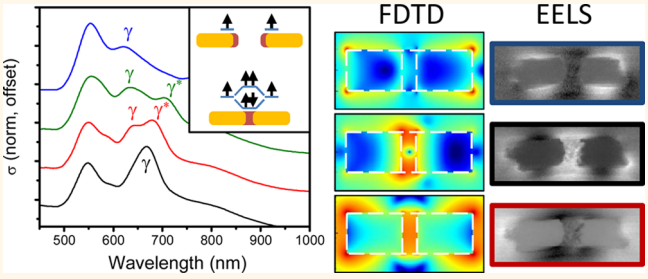

KEYWORDS: localized surface plasmon · hybrid nanoparticles · plasmon hybridization · dark-field spectroscopy · electron energy loss spectroscopy · nanogap antenna

Nanoscale plasmonic resonators localize optical energy below the diffraction limit and at high local intensities,[1] making them suitable for enhancing optical spectroscopy,[2−4] nonlinear optical processes,[5,6] optical energy conversion,[7,8] and joining the mismatched length-scales of optics and electronics. Recently, theoretical work has identified a new type of hybrid nanoresonator akin to a loaded-gap antenna, wherein the gap between two collinearly aligned metal nanorods is filled with a dielectric material.[9,10] The optical load provided by the gap material has a profound impact on the optical resonances supported by such a "nanogap" antenna, and thus provides an opportunity for modulation of antenna resonance at frequencies determined by the gap material's optical response.[5,11] Conversely, the antennas may be used to enhance or enable any field-driven function of the active gap material (semiconductor carrier generation, lasing or other emission, chemical catalysis, *etc.*).[12] More generally, metal—insulator—metal (MIM) systems have demonstrated near-perfect optical absorption,[13] immense radiative rate enhancements,[14] and independent tuning of the spectral response and modal intensity.[15]

While there is much interest in employing hybrid nanosystems to combine the field enhancements of plasmonic nanostructures with the utility of functional materials,[16] the spectral and spatial profiles of resonances supported on such heterostructures quickly become complex due to the interaction of the dielectric material with the metal,[17] mode hybridization,[18] activation of dark modes *via* symmetry-breaking,[19,20] and the

* Address correspondence to blake.simpkins@nrl.navy.mil.

Received for review March 13, 2015 and accepted May 11, 2015.

Published online May 11, 2015
10.1021/acsnano.5b01591

This article not subject to U.S. Copyright. Published 2015 by the American Chemical Society

nonideal morphologies inherent in structures made utilizing techniques at the forefront of nanofabrication.[21,15] The relatively simple nanogap antennas discussed in this manuscript contain only two Au rods joined by a dielectric gap material. However, substrate-induced degeneracy-lifting, mode coupling *via* near-field interactions, and mode hybridization are all active in these deceptively simple structures creating a rich spectral response which must be understood if hybrid resonators are to be adopted into industrial-scale, or even specialized, applications.

Hybrid systems have received a great deal of attention for photocatalysis[22,23] and, to a lesser extent, optical upconversion *via* wave mixing.[12,24] Many areas of technological impact (energy production, catalysis, and remediation) require production of large numbers of hybrid resonators whose resonant modes are both well-understood and tunable *via* conveniently accessible parameters. To this end, we have (i) used a high yield bottom-up technique, electrochemical deposition, to fabricate nanogap antennas comprising two Au nanorods joined by a CdS-filled gap, as well as the individual building block of these antennas (*i.e.*, single Au/CdS and pure Au rods) which serve to build a full understanding of the more complex structures; (ii) characterized the optical modes of individual antennas with polarization- and wavevector-controlled dark-field microscopy and microspectroscopy; (iii) mapped the spatial profiles of the dominant modes with electron energy loss spectroscopy and principal component analysis; (iv) utilized full-wave solutions of Maxwell's equations obtained with finite-difference time-domain (FDTD) simulations to reveal the nanoscopic origin of the radiating modes supported on such nanogap antennas. As with other elongated nanoplasmonic resonators,[25,26] our plasmonic nanogap antennas (Au/CdS/Au cylinders with typical lengths of 120/35/120 nm by ≈80 nm diameter) support transverse and longitudinal resonant modes, each with a different dependence on particle geometry (length, diameter, gap size) and dielectric environment (ambient, substrate, gap material). We find that there are two degenerate transverse modes (in- and out-of-plane near 570 nm) that are weakly split by the presence of the substrate,[17,27,28] and a longitudinal mode near 950 nm. In addition to these conventional modes, these loaded nanogap antennas also support a unique symmetry-forbidden gap-localized transverse mode which is the bonding mode arising from the splitting of degenerate transverse modes localized on the two gap faces. This mode is excitable in a conventional dark-field optical scattering geometry owing to a retardation effect, namely the phase difference experienced by the excitation wavefront as it travels the length of the gap, and can be spatially profiled using electron energy loss spectroscopy (EELS), which is sensitive to both bright and dark modes.[29] Furthermore, although not as intense as the conventional longitudinal mode, this previously unobserved mode is strong ($|E/E_0|^2 \approx 20$) and tightly localized in the nanoscopic (≈30 nm separation) gap region which would enable enhanced optical processes to be carried out in this dielectric load.

RESULTS AND DISCUSSION

Dark-Field Spectroscopy: Conventional Modes. The structures described herein, comprising two Au nanorods joined by a CdS gap material, are shown as-grown in the porous template in Figure 1a, and after release onto an ITO substrate in Figure 1b. Templated electrochemical deposition yields nanogap antennas at a density of $\approx 10^9$ cm^{-2}. While growth rates do vary from pore to pore, uniformity of 10–15% has been reported,[30] and the ability to mass-produce nanowires consisting of multiple dissimilar metal (Au, Ag, Ni, Fe, Cu, Pt, Pd, Al, *etc.*), polymer (polypyrrole,[31] polyaniline[32]), and semiconductor (CdS, CdTe, ZnO, ZnS, *etc.*) segments is truly unique. Two primary optical modes are supported on conventional, single component, plasmonic nanorods.

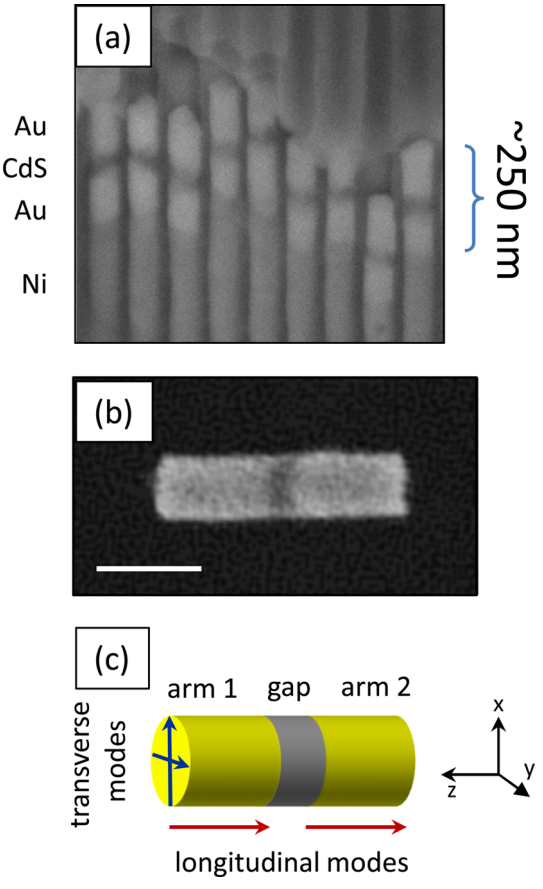

Figure 1. Introduction to nanogap antenna structure. (a) As-grown Au–CdS–Au heterostructures in the AAO template in which they were produced. Antennas were release, washed, and dropped (b) onto ITO/glass substrates for optical interrogation (100 nm scale bar). (c) The conventional transverse and longitudinal modes expected for such a structure.

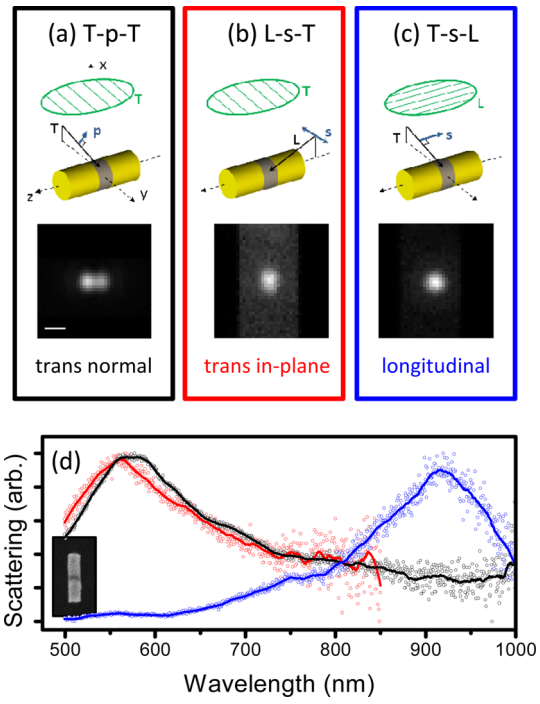

Figure 2. Subset of dark-field geometries illustrating example experimental conditions and resulting dipole images; (a) and (b) generate out-of-plane and in-plane oriented transverse dipoles, respectively, and (c) results in excitation of the longitudinal band. Spectra associated with these three geometries are plotted in (d) and reveal substrate-induced splitting of the degenerate transverse bands (black and red) as well as the much redder longitudinal band (blue). Inset to (d) is an SEM image of the nanogap antenna associated with all spectra and images in the figure. All dipole images have the same length scale and the scale bar in (a) is 500 nm.

These are transverse and longitudinal modes associated with charge oscillations in the radial and axial directions, respectively. Our hybrid nanogap antennas exhibit these two fundamental modes, modified to some degree by the substrate, as illustrated with blue and red arrows in Figure 1c, but our structures have *additional* gap-related modes which will be discussed later.

Figure 2 serves as an introduction to optical dark-field scattering in our structures and the modes excited therein. In addition to the high signal to background inherent in the dark-field experimental geometry, this method also offers great flexibility in modal excitation[33] and interrogation owing to its control of both incident and collection polarization as well as incident direction. If one limits consideration to only two principal directions, transverse and longitudinal (referred to as T and L), there are 2^3 combinations of experimental geometries. Three such geometries, along with their measured dipole radiation patterns, are illustrated in Figure 2. The nomenclature used to describe our experimental geometry consists of three terms which identify the direction of the incident k-vector, excitation polarization and collection polarization. Letters T and L are used to indicate transverse and longitudinal with respect to the antenna long axis. The excitation polarization is labeled as either s or p indicating an in-plane or out-of-plane excitation. For example, Figure 2a, depicts the T-p-T geometry. The first term, T in this case, indicates the k-vector of grazing incident light is restricted to be transverse to the nanowire. The second term, p, indicates that the excitation light is polarized normal to the substrate. The final term, another T in this case, labels the collection polarization (see Methods for further description). Because of the grazing angle of incidence, this condition excites a dipole oriented primarily normal to the substrate. The diffraction-limited image of such an out-of-plane dipole exhibits a donut shape that is radially polarized in the image plane.[34] However, when the collected light is first passed through a linear polarizer before being focused to an image, the donut is modified into a double-lobed feature oriented in the collection polarization direction, seen as the lobed scattering pattering in Figure 2a. The geometry of Figure 2b, L-s-T, also excites a transverse mode, but one that is oriented *in-plane* and nominally degenerate with the out-of-plane mode excited under T-p-T. These degenerate transverse modes correspond to the blue arrows in Figure 1c. The final example geometry, termed T-s-L in Figure 2c, excites a longitudinal in-plane dipole depicted as red arrows in Figure 1c. Both the transverse and longitudinal in-plane modes, Figure 2b,c, result in diffraction-limited Airy disks whose shapes are practically independent of collection polarization[34] (patterns shown in Figure 2b,c). The structures of the dark-field scattering images act to verify interpretation of the excited modes.

Optical scattering spectra associated with these three example geometries are given in Figure 2d and represent the conventional transverse- and longitudinal-modes supported by elongated antennas in general, and our nanogap antennas in particular. The first modification from the idealized case of a single-component nanorod in vacuum, a substrate-induced lifting of the degeneracy of the transverse modes, is experimentally observed as a splitting of the transverse mode (red and black curves in Figure 2d). This occurs for single plasmonic spheres[17] and rods[27] as well as our nanogap antennas. The transverse modes of a rod on a substrate are red-shifted due to the near-field of image dipoles created in the substrate, which reduce the restoring force of the radiated dipoles. The red-shift occurs for both the in-plane and out-of-plane transverse modes, but the interaction is much stronger for the out-of-plane geometry, leading to a larger red-shift and observable splitting whose magnitude increases with the optical index of the substrate.[17,27] For these nanogap antennas on ITO, the sign and approximate magnitude of this splitting were consistent among five nanowires tested (32 ± 16 nm wavelength splitting), and similar to the splitting observed for a conventional single component Au rod antenna (34 nm), included in the Supporting Information, Figure S1. We note that

the out-of-plane transverse dipole may be excited in either the T-p-T or L-p-T geometry (incident k along L, incident polarization out of plane, and detection polarization T). However, the L-p-T geometry also excites a "gap-localized transverse" mode arising from the coupling of transverse modes supported on both arms. We fully discuss this gap-localized transverse mode below, but use the simpler spectrum here to illustrate the transverse-mode splitting without the complication of another mode.

The longitudinal mode supported on a nanogap antenna is of particular interest due to the large gap-localized field enhancements associated with this mode and its potential to be modulated through active control of the gap material.[9,10] The longitudinal mode, ≈920 nm in Figure 2d, consists of in-phase oscillations present on *both* arms of the nanogap antenna. Longitudinal rod-resonances supported on conventional single-component Au rods may be tuned red with increasing rod length. In nanogap antennas, these oscillations may also couple through the end-to-end proximity of the antenna arms resulting in a red-shift of the longitudinal resonance supported on each single rod.[18] This red-shift increases with the gap optical index and with reduced separation ultimately reaching the resonance expected for a single rod of twice the length when the gap disappears. Although we observe a qualitative red-shifting of the longitudinal resonance with increased arm length, included in the Supporting Information as Figure S2, quantitative analysis regarding arm length and end-to-end coupling effects on the longitudinal resonance is difficult due to irregularities of rod end shapes and gap interface geometries, all of which influence longitudinal resonance position.[21] In particular, our simulations indicate that the rounding of the antenna arms near the gap region can reduce the longitudinal-mode shift with nominal antenna length. This is consistent with the previous work reported for air-gapped dipole antennas.[21] Other nonideal features such as protrusions into the gap region can produce a similar effect, although additional modes may appear in the scattering spectra. The imaging and spectroscopic results of Figure 2 confirm selective excitation of in-plane and out-of-plane transverse and longitudinal resonances and identify substrate-induced splitting of degenerate transverse modes in nanogap antennas. Dark-field spectra acquired for a full set of experimental geometries are included in the Supporting Information, Figure S3.

Dark-Field Spectroscopy: Symmetry Forbidden Gap-Localized Transverse Mode. To develop an understanding of the unique gap-localized transverse mode supported on these nanogap antennas, it is useful to inspect the modal building blocks of the system. We will now break our nanogap antennas into two simpler constituents, each a one-sided Au−CdS rod. For this, single Au rods were produced with CdS on one side and with lengths

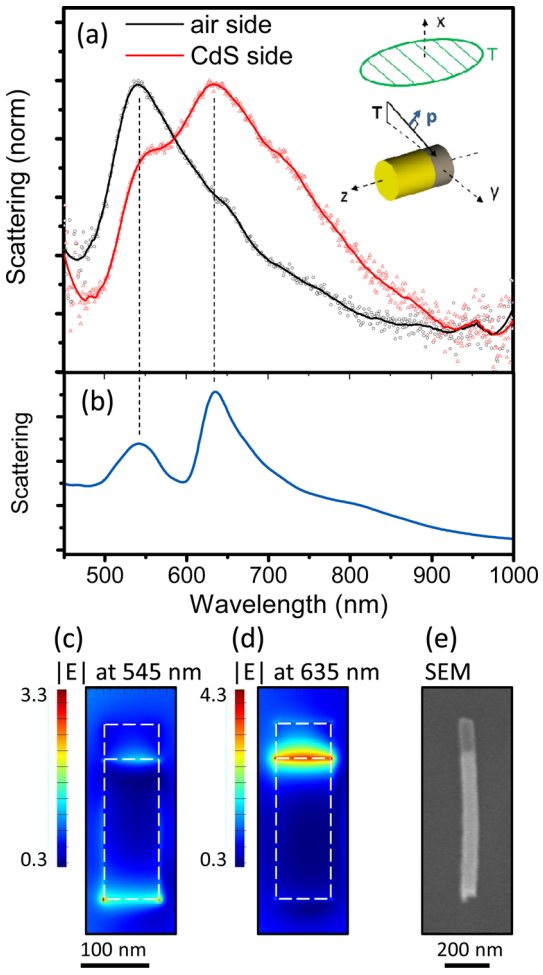

Figure 3. Scattering spectra and simulations of a one-sided Au−CdS rod. This structure represents a single arm building block of the full nanogap antenna. (a) Scattering spectra show the transverse mode near the CdS-capped end (red curve) exhibits a peak red-shifted relative to the transverse mode supported on the air-side of the rod (black curve). Inset illustrates experimental geometry. (b) Calculated spectrum for excitation light traveling along the rod (*k* along *z*) reproduces these same two resonances. Computed field distributions in the *y*−*z* plane at the middle of the rod identify the ≈545 nm mode as the conventional transverse mode localized at the bare end of the wire (c) and the red-shifted resonance as localized at the CdS-side of the rod (d). (e) SEM image of the rod used to generate (a).

long enough (≈1 μm) to spatially resolve the scattering spectra originating at each end of the rod. These rods were excited at grazing incidence from the transverse direction (Figure 3a inset). Scattered light was collected through an objective and sent to an imaging spectrometer enabling scattering from each end to be distinguished. Such Au rods will support transverse modes; however, the transverse modes at the two ends will resonate at different spectral positions due to the differing dielectric environments of the air *versus* the CdS side. The mode localized near the CdS side is expected to resonate at a longer wavelength by analogy with the Au nanosphere, which resonates at $\varepsilon_{Au} = -2\varepsilon_m$, where ε_m is the permittivity of the surrounding medium.

Results for such a structure are presented in Figure 3. Here, a single Au−CdS rod was evaluated in the T-p-T geometry which excites an out-of-plane transverse mode. (The L-s-T geometry excites an in-plane transverse mode which also generates the same insight, though the scattering strength of the L-s-T geometry is substantially weaker due to partially canceling radiation fields from the antialigned primary and image-charge dipoles.) Spectra from the two ends, Figure 3a, are distinctly different. The air-side transverse mode (black curve) displays a resonance at ∼550 nm, near the Au sphere resonance. The scattering spectrum from the CdS-side (red curve) exhibits a resonance at ∼630 nm, red-shifted due to the higher permittivity of the CdS. There is also a distinct shoulder at ∼550 nm associated with portions of the rod not in the immediate vicinity of the CdS cap. These resonances are explained by full wave simulations of a similar one-sided Au−CdS structure lying on a substrate. Grazing incidence excitation is approximated with light incident in-plane toward the antenna. The simulated spectra, Figure 3b, are dominated by two peaks similar to the experimental spectra. The field distributions associated with each of these peaks clearly shows the red-shifted mode (∼630 nm) localized at the CdS side (Figure 3d) and the unperturbed mode (≈550 nm) primarily associated with the air side, though there is some intensity near the CdS (Figure 3c). Also of note is the increased field strength predicted for the CdS side mode ($4.3E_0$) compared to the air side mode ($3.3E_0$). The larger field enhancement at the longer resonance wavelength is due largely to the smaller value of Im(ε) and field concentration expected in the higher index dielectric material. With this groundwork, we will next see how a symmetry-forbidden gap-localized transverse mode is formed through splitting of the two CdS-side transverse modes supported on the two arms of a nanogap antenna into bonding and antibonding modes.

Optical scattering spectra from several nanogap antennas of varying gap size, acquired under the L-p-T geometry, are presented in Figure 4a. This geometry excites the out-of-plane transverse mode with light incident along the rod axial direction, see inset. These spectra are dominated by a strong ≈580 nm transverse mode; however, there is a clear shoulder (labeled with arrows), which shifts red and increases in strength as gap size is reduced, eventually becoming a substantial second peak ≈800 nm. We attribute this feature to the lower energy branch of a splitting of the neighboring CdS-side transverse modes supported on the two arms of the antenna and accordingly refer to it as a *gap-localized transverse* mode. Although this type of mode has been theoretically predicted,[35] we find its description missing in the literature, even for similar systems.[36] Full wave simulations, Figure 4b−d, support this interpretation. Simulated spectra for gap sizes that cover the range measured in Figure 4a are shown in

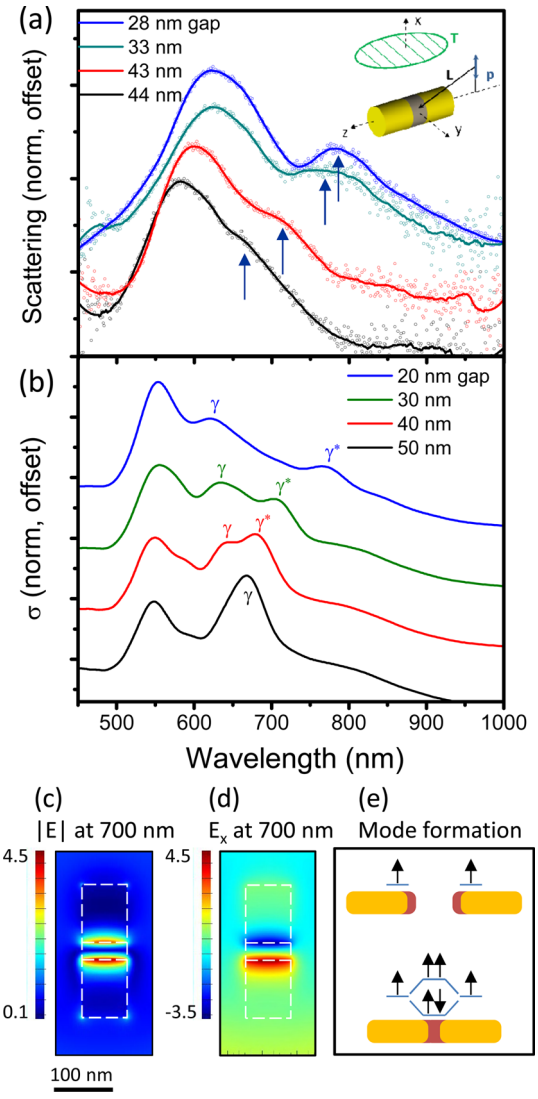

Figure 4. (a) Experimental and (b) simulated scattering spectra of the out-of-plane transverse mode as a function of gap size revealing a mode, γ*, which we attribute to the lower branch of split CdS-side transverse modes. (c and d) Field profiles for a 100/30/100 nm Au/CdS/Au structure taken through the $y-z$ plane at midwire, indicating that the γ* mode consists of antialigned dipoles. Mode splitting is illustrated in (e) showing the formation of aligned (bonding) and antialigned (antibonding) modes.

Figure 4b. These spectra reveal two peaks for large gap sizes (Figure 4b, black curve), one associated with the air-side (ends) of the antenna and the other with the CdS-filled gap. As gap size is reduced, the CdS-gap transverse mode splits into two modes, labeled γ and γ* in Figure 4b. Although our experimental results, broadened by (i) geometric nonidealities, (ii) a possibly larger value for the imaginary part of the Au permittivity, and (iii) the grazing rather than perfectly in-plane angle of incidence do not resolve all of the peaks predicted by simulation, they do clearly reveal the red-shifting lower branch of the gap-localized transverse mode, γ*. We believe the high energy branch is obscured under the dominant and broad transverse

mode[37] at ≈550 nm. Field profiles of γ^* are shown in Figure 4c,d for a gap size of 30 nm and reveal several critical aspects of this mode. It is highly localized at the gap interfaces, with field magnitudes reaching $\approx 4.5E_0$. However, more interesting is the fact that the sign of the field flips between one gap interface and the other, as shown in Figure 4d. This picture of antialigned dipoles residing at the gap interfaces lends support to the hypothesis that this mode is formed through hybridization of neighboring out-of-plane transverse modes as illustrated in Figure 4e. Mixing of two transverse modes would yield states of two dipoles either coaligned (high energy) or antialigned (low energy).[18,38] The lower energy case would shift to even lower energy with reduced gap, as we observe experimentally and theoretically, and be composed of antialigned dipoles, in agreement with our computational results. Field profiles for the blue branch, γ (Supporting Information Figure S4), indicate a mode localized at the gap and dominated by fields of only one sign, again, in agreement with our assignment of the γ and γ * peaks to the high and low energy modes formed through splitting of the transverse mode localized at the CdS−Au interface.

An interesting question arises here. For excitation by a uniform optical field, the antialigned γ^* mode is symmetry-forbidden when excited at a wavelength much larger than the nanostructure. However, we consider the incident wavefront approaching the nanogap antenna end-on. As the excitation wave propagates along the length of the rod, its phase varies with distance owing to retardation. Accounting for the optical index of CdS, the incident light travels $\sim 0.12\lambda$ across the gap (for 30 nm gap at $\lambda = 625$ nm). Although a small fraction of the total wavelength, this is about 1/4 of the $\lambda/2$ needed to optimally excite the antialigned modes. We propose that the phase difference experienced by the two gap interfaces is sufficient to excite this symmetry-forbidden gap-localized transverse mode. Excitation of higher order modes has been predicted as particle size increases, in part, due to phase variation across the particle.[39] If our proposition is correct, excitation of this mode should be impossible with light incident from the transverse direction since the wavefront's phase would be identical at the two gap interfaces. Indeed, both theoretical and experimental results confirm this hypothesis. The theoretical results presented in Figure 5a show scattering cross sections for a 30 nm gap structure excited in two geometries. As proposed above, the light incident along the nanowire axial direction (red) excites the lower branch, γ^*, while transverse incident light (black) only excites γ. Experimental results, though broadened to the point of obscuring the γ peak, do verify the presence (absence) of the γ^* feature for the L-p-T (T-p-T) geometry, Figure 5b. This behavior suggests a trade-off between the γ−γ^* splitting magnitude and

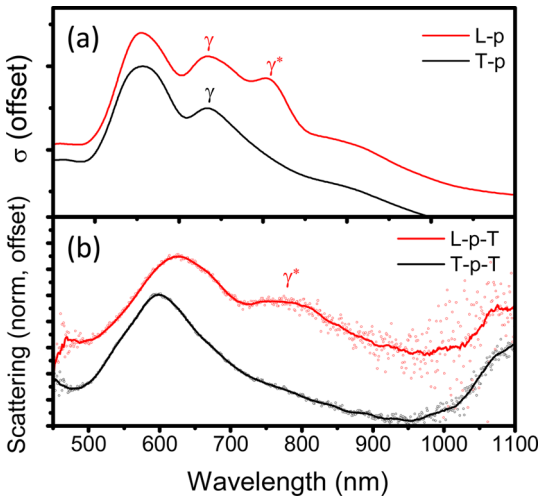

Figure 5. (a) Simulated and (b) measured scattering spectra for probe light incident longitudinal to the nanoantenna axis (red) and transverse to it (black). These results verify that the mode, γ^*, is only excited when light is incident along the longitudinal direction,. This is consistent with this mode being composed of antialigned dipoles. Simulated spectra are calculated without collection polarization.

the interaction strength of the γ^* mode and the excitation light field. We have shown that the splitting increasing with decreased gap size but the ability to excite this mode, driven by the phase difference at the two gap interfaces, would diminish with decreasing gap size. When utilizing such a system, one would have to balance the spectral tuning requirements of the γ^* mode while maintaining the ability to optically couple to it.

Electron Energy Loss Spectroscopy and Imaging. The theoretical and far-field optical results above paint an intriguing picture of a gap-localized mode which red-shifts as gap size decreases. To directly image the different modes supported on our nanogap antennas, we EELS on antennas drop cast on a variety of membrane supports. Importantly for this study, EELS combines nanoscale spatial resolution with the ability to excite optically forbidden modes[29] such as the gap-localized transverse mode described above. EELS has found great utility in imaging plasmonic modes supported on metal spheres[40] and rods,[41,42] air-gapped nanostructures,[29] and waveguide structures.[43] However, very few reports[44] explore hybrid nanostructures which incorporate high-index dielectrics as integral components of the structure as we show here.

Candidate antenna structures were first identified by high-angle annular dark-field scanning transmission electron microscopy (HAADF-STEM), and then characterized by spectrum imaging of the localized surface plasmon resonance region of the EEL spectrum, wherein a loss spectrum is recorded for every image pixel. After pixel-by-pixel fitting and subtraction of a power-law background, principal component analysis (PCA) was applied to the spectrum image data to identify the

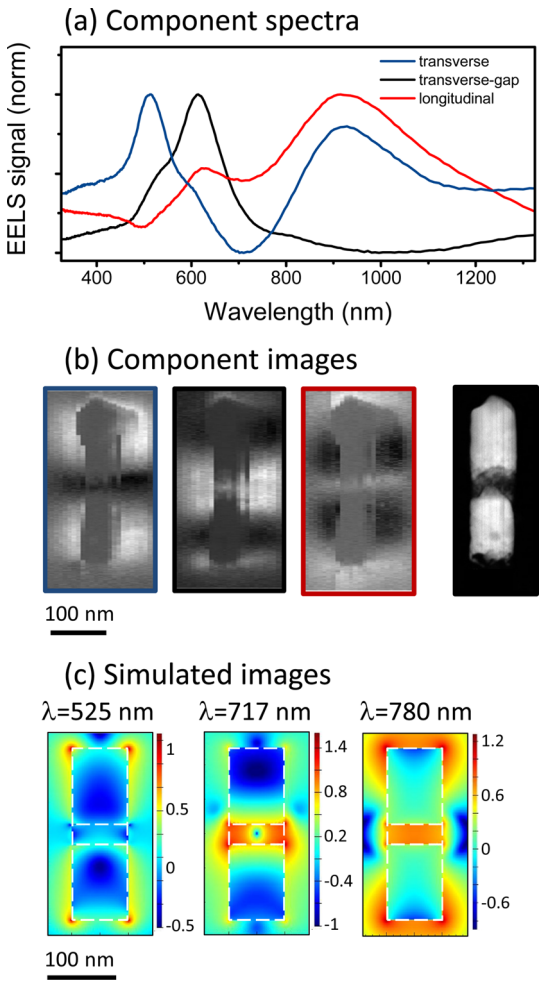

Figure 6. (a) Component spectra extracted from EEL spectra of antenna on SiN_x membrane and 150 kV accelerating voltage revealing three dominant modes which we assign to conventional transverse (blue), gap-localized transverse (black), and longitudinal (red) modes. (b) Images produced from the principal component spectra in (a) as well as a TEM image of the nanogap antenna show the spatial distribution of each mode. (c) FDTD optical simulations showing $|E|$ profiles associated with the three modes for a 110/30/110 nm Au/CdS/Au structure plotted on a logarithmic scale. These simulated profiles correlate well with the experimental images of (b).

spatial extent of spectrally distinct plasmon resonances. In PCA as used here, the "principal components" are the singular value decompositions of a matrix which contains all spectra from the entire field-of-view. A typical EEL spectral decomposition for a nanogap antenna is presented in Figure 6a (30 nm thick SiN_x membrane, 150 kV accelerating voltage), with three component modes identified.

Consistent with the far-field optical scattering results, EELS analysis reveals the same three strong modes: the conventional transverse (≈550 nm), the gap-localized transverse (≈625 nm), and the longitudinal (≈950 nm). These resonances are slightly bluer than those observed for nanostructures on ITO/glass, presumably due to the weaker dielectric environment associated with the thin TEM supports used for EELS. For the sample set here (diameters from ≈65 to 80 nm and single arm lengths from ≈100 to 130 nm), the spectral position of the conventional transverse mode is only weakly dependent on geometry, while the longitudinal mode is shown to vary from ~850 to 1000 nm. These behaviors are qualitatively consistent among nine nanogap antennas (remainder of the data sets presented in Supporting Information, Figure S5). Spatial maps constructed from the principal component basis-set are shown in Figure 6b, along with a HAADF-STEM image. To generate each component image, pixel intensity is given by the weighting value associated with that particular component spectrum. The first of the three EELS images (associated with blue curve in Figure 6a) shows a conventional transverse mode along the outer surface of the antenna arms. The second mode (symmetry-forbidden gap-localized transverse mode, associated with the black curve) is primarily localized in the gap, and the final component (longitudinal mode, associated with the red curve) is strongest at the antenna ends, with some intensity at the gap as well. As a comparison, images of local in-plane electric fields of similar structures generated by full wave finite-difference time-domain (FDTD) simulations of optically excited modes are shown in Figure 6c. The spatial distribution of the modes predicted from simulation match well with the experimental images in Figure 6b, and indicate consistency between the optical dark-field and EELS results. Furthermore, these EELS results provide direct experimental evidence that the mode assigned as the gap-localized transverse mode, based on dark-field optical results, is indeed localized in the gap region (black curve in Figure 6a and black framed image in Figure 6b). In comparing the component spectra, we note some spatial and spectral overlap between modes. For instance, the conventional transverse mode (blue) contains a peak in the vicinity of the longitudinal mode (≈950 nm) and the longitudinal mode (red) contains a small contribution associated with the gap-localized transverse mode (≈620 nm). These convolutions occur as a result of the spatially neutral treatment of spectra with PCA. As shown in the theoretical results of Figure 6c, the conventional transverse and gap-localized transverse modes both have some intensity at the antenna arm exterior near the gap. Without spatial constraints, PCA will not spectrally distinguish modes which reside at the same spatial location. The same is true for the longitudinal mode, which has some intensity in the gap causing colocalization between the longitudinal and gap-localized transverse modes. But even without spatial constraints, PCA of the EELS data sets reveal the spatial extent of specific modes on loaded nanogap antennas.

We also conducted EELS experiments using lacey carbon substrates and a larger (300 keV) primary beam energy. A typical data set is presented in Figure 7a,b. These results are entirely consistent with those

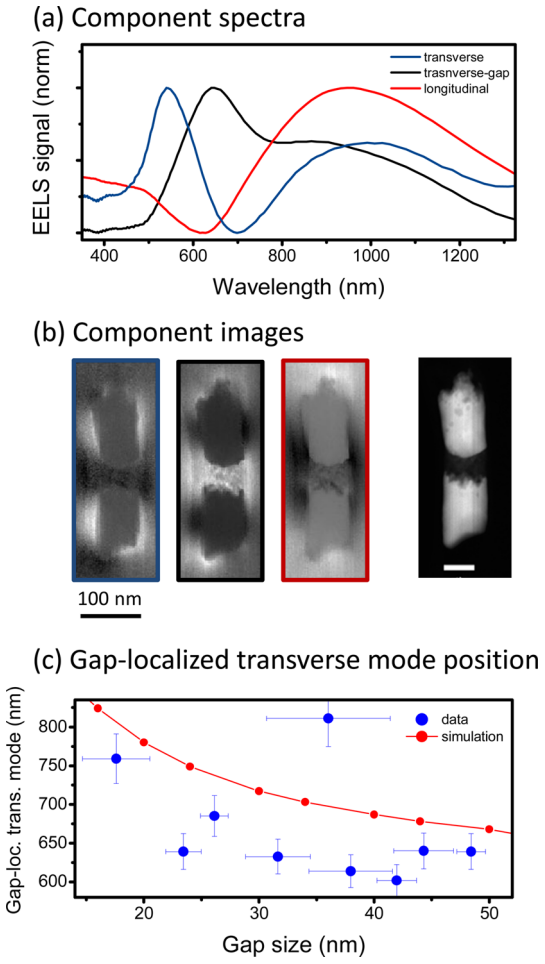

Figure 7. (a) Component spectra extracted from EELS data for antenna on lacy carbon support acquired at 300 kV accelerating voltage and (b) images produced from the principal component spectra in (a) as well as a TEM image of the nanogap antenna. (c) Spectral center of gap-localized transverse mode (blue) extracted from EELS data as a function of gap size showing modal red-shift with decreased gap. Simulated mode position is also presented (red).

presented in Figure 6 (three primary components associated with the conventional transverse, gap-localized transverse, and longitudinal modes), and demonstrate the robustness of the results with respect to substrate choice and accelerating voltage, despite the smaller electron−plasmon interaction cross section expected at the higher beam voltage.[45] As in the DF optical investigation, the EELS resonance attributed to the gap-localized transverse mode shifts from antenna to antenna. To test if gap-size is responsible, as was found in the far-field optical results (Figure 4), we plot in Figure 7c the peak position of the gap-localized transverse mode (*i.e.*, the black spectrum in Figure 7a) as a function of the gap size measured as described in Methods. A clear correlation between gap size and gap-localized transverse mode position is evident, with this mode shifting red (from $\lambda \approx 600$ to 820 nm) as the gap size decreased (from ≈53 to 24 nm). This indicates the gap-localized transverse mode is sensitive to interaction between the two neighboring gap interfaces and reinforces our claim that it arises due to hybridization of transverse modes separated by a dielectric. There is a single outlying data point associated with an antenna whose gap exhibits a large protrusion (see detail in Figure S5d). Correlation between gap size and gap-localized transverse mode position is further supported by noting the simulation results (red symbols and line). The simulated spectra used to generate these spectral positions is included in the Supporting Information (Figure S6a). Lastly, we note our simulations predict that the gap-localized transverse mode disappears when the CdS gap material is replaced by air for gaps larger than ≈10 nm (see Supporting Information Figure S6b). This further strengthens our claim that the gap-localized transverse mode we observe arises due to coupling between transverse modes supported on adjacent antenna arms, which would be enhanced for larger gap dielectric constants.[46]

CONCLUSION

Through the combination of far-field optical microscopy and electron energy-loss spectroscopy and imaging, we have spectrally and spatially characterized the optical resonances supported on loaded nanogap antennas. We identify a "dark" mode, forbidden in the dipole approximation, which arises from a hybridization between two transverse modes supported on each arm of the antenna. This *gap-localized transverse* mode is confined to the gap load, enabling (i) delivery of substantial energy to the gap material and (ii) the possibility of tuning the antenna resonant-wavelength *via* active modulation of the gap material's optical properties. This mode is sensitive to both the gap geometry (tuning red with decreased gap size) and gap dielectric response (the mode effectively disappears for an air-gap structure). Hybrid nanostructures consisting of plasmonic and semiconducting components, such as those discussed here, have potential for active resonators and for multifunctional applications such as plasmonically enhanced catalysis or nonlinear optical processes, but only after spectral and spatial modal profiles are understood and controlled.

METHODS

Material Synthesis. Nanogap antennas were prepared by templated electrochemical deposition of Au and CdS. Details are presented elsewhere,[47] but briefly, nickel-backed anodized alumina (AAO) templates were immersed in a 3-electrode electrochemical cell filled with the appropriate deposition solution. Galvanostatic electrodeposition of sacrificial Ni was followed by that of the active structure consisting of Au, CdS, and finally Au.

After each layer is deposited into the porous template, the cell is emptied, rinsed, and refilled with the next deposition solution.[30] Deposition solutions were Technic, Inc.'s Orotemp24 with 0.5% TritonX405 surfactant for Au and 55 mM $CdCl_2$, 190 mM elemental S, and 0.5 vol % TritonX405 in dimethyl sulfoxide for CdS. This procedure results in Au/CdS/Au heterostructures with nominal lengths of 110/30/110 nm for the respective Au/CdS/Au regions with a diameter measured to be 73 ± 5 nm as defined by the AAO template. TEM imaging and electron diffraction was used to identify the gap material as CdS.[47] As-deposited structures residing in the deposition template are pictured in Figure 1a. The Ni backing was selectively etched in hydrochloric acid, and then the template was removed *via* wet etching (1 M NaOH) and the wires were washed three times in DI H_2O and finally suspended in 1:1 H_2O/isopropyl alcohol. Nanogap antennas were then drop-dried from solution onto ITO-coated coverslips (Figure 1b) for dark-field measurements and various TEM supports (lacy carbon, electron-transparent SiN_x and Si membranes). Antennas were located and imaged *via* scanning electron microscopy before optical measurements to verify structure geometry.

Optical Spectroscopy. Dark-field (DF) imaging and spectroscopy were carried out on a modified inverted microscope with a commercial DF objective (Nikon, 100×, 0.9 numerical aperture) that directed the incident halogen light-source onto the sample at glancing 79° relative to normal and collected light scattered at 0−64° relative to normal. Spectra and micrographs were recorded with an imaging spectrometer (Acton SpectraPro 2300) equipped with a switchable mirror (for images) and grating (for spectra). Sensitivity was enhanced by attaching the spectrometer directly to a side port of the microscope and by using a thermoelectrically cooled electron-multiplying charge-coupled device (Andor Newton 971). The incident wavevector, *k*, of the light was restricted with a mask placed in the illumination path, and both incident and collected light were polarization-controlled. As illustrated in Figure 2a−c, we notate the scattering geometry by using a three-term shorthand, for example (T-s-L), to convey, in order, the incident k-direction, excitation orientation, and collected polarization. T and L stand for transverse and longitudinal with respect to the antenna long axis and s or p indication in-plane or out-of-plane excitation polarization. For instance, (T-s-L) indicates a *k* vector transverse to the antenna, excitation polarization in-plane, and collection polarization oriented longitudinal with respect to the nanogap antenna axial direction. All dark-field spectral data presented include the raw data (dots) and data smoothed *via* a Savitsky−Golay algorithm (solid curves of the same color).

Electron Energy Loss Spectroscopy and Imaging. High resolution spatial profiles of the resonant modes of the antennae were acquired using electron energy loss (EEL) spectroscopy and imaging with a FEI Titan, spherical-aberration corrected scanning transmission electron microscope (STEM) with a monochromated source (150 meV full-width half-max zero-loss peak in vacuum, using 13 mrad). Samples were sonicated into solution and drop cast on SiO_x, carbon, and SiN_x support films. Following identification of candidate structures by high- angle annular dark-field (HAADF) STEM imaging, EELS images were acquired pixel-by-pixel (with 2 nm pixel size). Postprocessing of the EEL spectra included (i) centering each spectrum on its zero-loss-peak (ZLP) maximum, (ii) fitting and subtracting a power law background function to energy regions below and above the region of spectral interest, (iii) removing the zero-loss peak, and finally running a principal component analysis (PCA) to identify the most prominent resonant modes. PCA was carried out on the subtracted spectral data without spatial weighting constraints. Principal components are identified by finding the intersection of an exponential fit to the maximum value in the first several component spectra and a linear fit to the slowly decaying values of the higher order component spectra. Resonances whose centers overlap spectrally to within the full-width, half-maximum energy of the zero-loss peak are combined. Gap size was measured with the Matlab software package as follows. Dark-field TEM images were thresholded enabling automated locating of gap interfaces. Averages and standard deviations were generated by measuring gap distance for ≈100 positions along the interface.

Simulation. Full wave simulations of the nanogap antennas lying on a 90 nm ITO layer on glass substrate were carried out using a commercial finite-difference time-domain (FDTD) software package provided by Lumerical. The calculations were performed using the total-field scattered-field (TFSF) source. The geometry of the DF optical experiments was closely approximated by directing the incident light parallel to the substrate either along or perpendicular to the antenna axis. All electric field magnitudes are normalized to that of the incident plane wave. Incident polarization was limited to be in-plane or out-of-plane and no analyzer polarization was applied. The mesh pitch around the antennas was set to 1 nm. To enable the excitation with the TFSF source parallel to the substrate, the antenna structure and the substrate are separated by a vacuum gap of 4 nm.[48] This is needed because the boundaries of the TFSF region perpendicular to the incident field must be in the same material, and no monitors can cross the TFSF boundaries. By also performing the simulations in the geometry with normal incidence, we find that the required separation between the substrate and the antenna causes a small blue shift of ≈5 nm for the transverse mode. The scattered intensity above the substrate was recorded with a field monitor without polarization analysis, and the collection cone of the microscope objective was approximately modeled by adjusting the lateral extent of the monitor so that a similar light cone can be collected. In almost all cases, the total scattering cross section displayed a very similar behavior. The red shift of the peak of the scattering cross section from the peak of the extinction cross section was found to be no larger than 10 nm in nearly all cases.[49,50] The field profiles around the antennas were also monitored at the wavelengths corresponding to the peaks of the scattering spectra. The simulations were repeated for the case without a substrate, and a blue shift of ≈20 nm was observed for the transverse mode.

Conflict of Interest: The authors declare no competing financial interest.

Acknowledgment. We thank Professor Sang Bok Lee for providing the fine-pore anodic alumina templates in which the nanostructures were produced. Research was funded by the Office of Naval Research Nanoscience Institute program 61-P087-13.

Supporting Information Available: Resonant modes of single gold rod; longitudinal mode dispersion with length; full set of optical dark field scattering data; field distributions associated with γ and γ^* branches; full set of EELS data; gap-dependent position of gap-localized transverse mode. The Supporting Information is available free of charge on the ACS Publications website at DOI: 10.1021/acsnano.5b01591.

REFERENCES AND NOTES

1. Novotny, L.; van Hulst, N. Antennas for Light. *Nat. Photoincs* **2011**, *5*, 83.
2. Haynes, C. L.; Van Duyne, R. P. Nanosphere Lithography: A Versatile Nanofabrication Tool for Studies of Size-Dependent Nanoparticle Optics. *J. Phys. Chem. B* **2001**, *105*, 5599–5611.
3. Caldwell, J. D.; Glembocki, O. J.; Bezares, F. J.; Kariniemi, M. I.; Niinistö, J. T.; Hatanpää, T. T.; Rendell, R. W.; Ukaegbu, M.; Ritala, M. K.; Prokes, S. M.; Hosten, C. M.; Leskelä, M. A.; Kasica, R. Large-Area Plasmonic Hot-Spot Arrays: Sub-2 nm Interparticle Separations with Plasma-Enhanced Atomic Layer Deposition of Ag on Periodic Arrays of Si Nanopillars. *Opt. Express* **2011**, *19*, 26056–26064.
4. Kabashin, A. V.; Evans, P.; Pastkovsky, S.; Hendren, W.; Wurtz, G. A.; Atkinson, R.; Pollard, R.; Podolskiy, V. A.; Zayats, A. V. Plasmonic Nanorod Metamaterials for Biosensing. *Nat. Mater.* **2009**, *8*, 867–871.
5. Kauranen, M.; Zayats, A. V. Nonlinear Plasmonics. *Nat. Photonics* **2012**, *6*, 737–748.
6. Pu, Y.; Grange, R.; Hsieh, C. L.; Psaltis, D. Nonlinear Optical Properties of Core-Shell Nanocavities for Enhanced Second-Harmonic Generation. *Phys. Rev. Lett.* **2010**, *104*, 207402.

7. Schaadt, D. M.; Feng, B.; Yu, E. T. Enhanced Semiconductor Optical Absorption *via* Surface Plasmon Excitation in Metal Nanoparticles. *Appl. Phys. Lett.* **2005**, *86*, 063106.
8. Ferry, V. E.; Sweatlock, L. A.; Pacifici, D.; Atwater, H. A. Plasmonic Nanostructure Design for Efficient Light Coupling into Solar Cells. *Nano Lett.* **2008**, *8*, 4391–4397.
9. Alù, A.; Engheta, N. Tuning the Scattering Response of Optical Nanoantennas with Nanocircuit Loads. *Nat. Photonics* **2008**, *2*, 307–310.
10. Large, N.; Abb, M.; Aizpurua, J.; Muskens, O. L. Photoconductively Loaded Plasmonic Nanoantenna as Building Block for Ultracompact Optical Switches. *Nano Lett.* **2010**, *10*, 1741–1746.
11. Stockman, M. I. Nanoplasmonics: Past, Present, and Glimpse into Future. *Opt. Express* **2011**, *19*, 22029–22106.
12. Aouani, H.; Rahmani, M.; Navarro-Cia, M.; Maier, S. A. *Nat. Nanotechnol.* **2014**, *9*, 290.
13. Alaee, R.; Menzel, C.; Huebner, U.; Pshenay-Severin, E.; Bin Hasan, S.; Pertsch, T.; Rockstuhl, C.; Lederer, F. Deep-Subwavelength Plasmonic Nanoresonators Exploiting Extreme Coupling. *Nano Lett.* **2013**, *13*, 3482–3486.
14. Akselrod, G. M.; Argyropoulos, C.; Hoang, T. B.; Ciracì, C.; Fang, C.; Huang, J.; Smith, D. R.; Mikkelsen, M. H. Probing the Mechanisms of Large Purcell Enhancement in Plasmonic Nanoantennas. *Nat. Photonics* **2014**, *8*, 835–840.
15. Esteban, R.; Aguirregabiria, G.; Borisov, A. G.; Wang, Y. M.; Nordlander, P.; Bryant, G. W.; Aizpurua, J. The Morphology of Narrow Gaps Modifies the Plasmonic Response. *ACS Photonics* **2015**, *2*, 295–305.
16. Zayats, A. V.; Maier, S. A., Eds.; *Active Plasmonics and Tuneable Plasmonic Metamaterials*; John Wiley & Sons, Inc.: Hoboken , NJ, 2013.
17. Knight, M. W.; Wu, Y.; Lassiter, J. B.; Nordlander, P.; Halas, N. J. Substrates Matter: Influence of an Adjacent Dielectric on an Individual Plasmonic Nanoparticle. *Nano Lett.* **2009**, *9*, 2188–2192.
18. Jain, P. K.; El-Sayed, M. A. Plasmonic Coupling in Noble Metal Nanostructures. *Chem. Phys. Lett.* **2010**, *487*, 153–164.
19. Verellen, N.; Sonnefraud, Y.; Sobhani, H.; Hao, F.; Moshchalkov, V. V.; Dorpe, P. V.; Nordlander, P.; Maier, S. A. Fano Resonances in Individual Coherent Plasmonic Nanocavities. *Nano Lett.* **2009**, *9*, 1663–1667.
20. Zhang, Z.; Weber-Bargioni, A.; Wu, S. W.; Dhuey, S.; Cabrini, S.; Schuck, P. J. Manipulating Nanoscale Light Fields with the Asymmetric Bowtie Nano-Colorsorter. *Nano Lett.* **2009**, *9*, 4505–4509.
21. Portela, A.; Yano, T.; Santschi, C.; Matsui, H.; Hayashi, T.; Hara, M.; Martin, O. J. F.; Tabata, H. Spectral Tunability of Realistic Plasmonic Nanoantennas. *Appl. Phys. Lett.* **2014**, *105*, 091105.
22. Christopher, P.; Xin, H.; Andiappan, M.; Linic, S. Singular Characteristics and Unique Chemical Bond Activation Mechanisms of Photocatalytic Reactions on Plasmonic Nanostructures. *Nat. Mater.* **2012**, *11*, 1044.
23. Liu, Z.; Hou, W.; Pavaskar, P.; Aykol, M.; Cronin, S. B. Plasmon Resonant Enhancement of Photocatalytic Water Splitting Under Visible Illumination. *Nano Lett.* **2011**, *11*, 1111–1116.
24. Chen, P.-Y.; Argyropoulos, C.; Alu, A. Enhanced Nonlinearities Using Plasmonic Nanoantennas. *Nanophotonics* **2012**, *1*, 221–233.
25. Bryant, G. W.; García de Abajo, F. J.; Aizpurua, J. Mapping the Plasmon Resonances of Metallic Nanoantennas. *Nano Lett.* **2008**, *8*, 631–636.
26. Pérez-Juste, J.; Pastoriza-Santos, I.; Liz-Marzán, L. M.; Mulvaney, P. Gold Nanorods: Synthesis, Characterization and Applications. *Coord. Chem. Rev.*, *249*, 1870−1901; 36th International Conference on Coordination Chemistry, Merida, Mexico, July 2004.
27. Albella, P.; Moreno, F.; Saiz, J. M.; González, F. Surface Inspection by Monitoring Spectral Shifts of Localized Plasmon Resonances. *Opt. Express* **2008**, *16*, 12872–12879.
28. Chen, H.; Shao, L.; Ming, T.; Woo, K. C.; Man, Y. C.; Wang, J.; Lin, H.-Q. Observation of the Fano Resonance in Gold Nanorods Supported on High-Dielectric-Constant Substrates. *ACS Nano* **2011**, *5*, 6754–6763.
29. Koh, A. L.; Bao, K.; Khan, I.; Smith, W. E.; Kothleitner, G.; Nordlander, P.; Maier, S. A.; McComb, D. W. Electron Energy-Loss Spectroscopy (EELS) of Surface Plasmons in Single Silver Nanoparticles and Dimers: Influence of Beam Damage and Mapping of Dark Modes. *ACS Nano* **2009**, *3*, 3015–3022.
30. Osberg, K. D.; Rycenga, M.; Harris, N.; Schmucker, A. L.; Langille, M. R.; Schatz, G. C.; Mirkin, C. A. Dispersible Gold Nanorod Dimers with Sub-5 nm Gaps as Local Amplifiers for Surface-Enhanced Raman Scattering. *Nano Lett.* **2012**, *12*, 3828–3832.
31. Jérôme, C.; Jérôme, R. Electrochemical Synthesis of Polypyrrole Nanowires. *Angew. Chem., Int. Ed. Engl.* **1998**, *37*, 2488–2490.
32. Liu, H.; Kameoka, J.; Czaplewski, D. A.; Craighead, H. G. Polymeric Nanowire Chemical Sensor. *Nano Lett.* **2004**, *4*, 671–675.
33. Albella, P.; Garcia-Cueto, B.; González, F.; Moreno, F.; Wu, P. C.; Kim, T.-H.; Brown, A.; Yang, Y.; Everitt, H. O.; Videen, G. Shape Matters: Plasmonic Nanoparticle Shape Enhances Interaction with Dielectric Substrate. *Nano Lett.* **2011**, *11*, 3531–3537.
34. Novotny, L.; Hecht, B. *Principles of Nano-Optics*; Cambridge University Press: New York, 2006.
35. Nordlander, P.; Oubre, C.; Prodan, E.; Li, K.; Stockman, M. I. Plasmon Hybridization in Nanoparticle Dimers. *Nano Lett.* **2004**, *4*, 899–903.
36. Alber, I.; Sigle, W.; Müller, S.; Neumann, R.; Picht, O.; Rauber, M.; van Aken, P. A.; Toimil-Molares, M. E. Visualization of Multipolar Longitudinal and Transversal Surface Plasmon Modes in Nanowire Dimers. *ACS Nano* **2011**, *5*, 9845–9853.
37. Abb, M.; Wang, Y.; Albella, P.; de Groot, C. H.; Aizpurua, J.; Muskens, O. L. Interference, Coupling, and Nonlinear Control of High-Order Modes in Single Asymmetric Nanoantennas. *ACS Nano* **2012**, *6*, 6462–6470.
38. Alonso-González, P.; Albella, P.; Golmar, F.; Arzubiaga, L.; Casanova, F.; Hueso, L. E.; Aizpurua, J.; Hillenbrand, R. Visualizing the Near-Field Coupling and Interference of Bonding and Anti-Bonding Modes in Infrared Dimer Nanoantennas. *Opt. Express* **2013**, *21*, 1270–1280.
39. Kelly, K. L.; Coronado, E.; Zhao, L. L.; Schatz, G. C. The Optical Properties of Metal Nanoparticles: The Influence of Size, Shape, and Dielectric Environment. *J. Phys. Chem. B* **2002**, *107*, 668–677.
40. Collins, S. M.; Midgley, P. A. Surface Plasmon Excitations in Metal Spheres: Direct Comparison of Light Scattering and Electron Energy-Loss Spectroscopy by Modal Decomposition. *Phys. Rev. B* **2013**, *87*, 235432.
41. Nelayah, J.; Kociak, M.; Stéphan, O.; Javier García de Abajo, F.; Tencé, M.; Henrard, L.; Taverna, D.; Pastoriza-Santos, I.; Liz-Marzán, L. M.; Colliex, C. Mapping Surface Plasmons on a Single Metallic Nanoparticle. *Nat. Phys.* **2007**, *3*, 348–353.
42. Guiton, B. S.; Iberi, V.; Li, S.; Leonard, D. N.; Parish, C. M.; Kotula, P. G.; Varela, M.; Schatz, G. C.; Pennycook, S. J.; Camden, J. P. Correlated Optical Measurements and Plasmon Mapping of Silver Nanorods. *Nano Lett.* **2011**, *11*, 3482–3488.
43. Raza, S.; Stenger, N.; Pors, A.; Holmgaard, T.; Kadkhodazadeh, S.; Wagner, J. B.; Pedersen, K.; Wubs, M.; Bozhevolnyi, S. I.; Mortensen, N. A. Extremely Confined Gap Surface-Plasmon Modes Excited by Electrons. *Nat. Commun.* **2014**, *5*, 1.
44. Dong, Z.; Bosman, M.; Zhu, D.; Goh, X. M.; Yang, J. K. W. Fabrication of Suspended Metal−Dielectric−Metal Plasmonic Nanostructures. *Nanotechnology* **2014**, *25*, 135303.
45. Egerton, R. F. *Electron Energy-Loss Spectroscopy in the Electron Microscope*, 2nd ed.; The language of science; Plenum Press: New York, 1996.
46. Jain, P. K.; Huang, W.; El-Sayed, M. A. On the Universal Scaling Behavior of the Distance Decay of Plasmon Coupling in Metal Nanoparticle Pairs: A Plasmon Ruler Equation. *Nano Lett.* **2007**, *7*, 2080–2088.

47. Simpkins, B. S.; Brintlinger, T. H.; Stroud, R. M.; Sherrill, S. A.; Lee, S. B.; Pehrsson, P. E. Controlling the Crystallinity of Electrochemically Deposited CdS Nanowires. *J. Phys. Chem. C* **2013**, *117*, 11843.
48. Wu, T.; Nordlander, P. Finite-Difference Time-Domain Modeling of the Optical Properties of Nanoparticles Near Dielectric Substrates. *J. Phys. Chem. C* **2010**, *114*, 7302.
49. Moreno, F.; Albella, P.; Nieto-Vesperinas, M. Analysis of the Spectral Behavior of Localized Plasmon Resonances in the Near- and Far-Field Regimes. *Langmuir* **2013**, *29*, 6715–6721.
50. Zuloaga, J.; Nordlander, P. On the Energy Shift between Near-Field and Far-Field Peak Intensities in Localized Plasmon Systems. *Nano Lett.* **2011**, *11*, 1280–1283.